Acta Materialia 269 (2024) 119810

Contents lists available at ScienceDirect

Acta Materialia

journal homepage: www.elsevier.com/locate/actamat

Full length article

Heterogeneous precipitate microstructure design in β-Ti alloys by regulating the cooling rate

Mengyuan Hao [a,b], Dong Wang [a,*], Yalong Wang [c], Tianlong Zhang [d], Pei Li [e], Yaning Guo [f], Yufeng Zheng [g,*], Qiaoyan Sun [a], Yunzhi Wang [h,*]

[a] Center of Microstructure science, Frontier Institute of Science and Technology, State Key Laboratory for Mechanical Behavior of Materials, Xi'an Jiaotong University, Xi'an 710049, China
[b] Northwest Institute for Non-ferrous Metal Research, Xi'an 710016, China
[c] Lanzhou Institute of Physics, Lanzhou 730000, China
[d] Department of Mechanical and Aerospace Engineering, Hong Kong University of Science and Technology, Hong Kong 999077, China
[e] Thermal Power Research Institute Co. Ltd., Xi'an 710032, China
[f] Shenzhen Clou Electronics Co., Ltd. Shenzhen 518057, China
[g] Department of Materials Science and Engineering, College of Engineering, University of North Texas, Texas 76207, USA
[h] Department of Materials Science and Engineering, The Ohio State University, Columbus, OH 43210, USA

ARTICLE INFO

Keywords:
Phase field simulation
Cooling rate
Heterogeneous precipitate microstructure
Classical nucleation and growth mechanism
Pseudospinodal mechanism

ABSTRACT

Cooling after solutionizing or aging plays a crucial role in heat treatment and can greatly influence the final precipitate microstructure and mechanical properties of titanium (Ti) alloys. In this study, we employ phase field simulations to strategically engineer heterogeneous precipitate microstructures in near β-Ti alloys by manipulating the cooling rate, which leads to different phase transition mechanisms. By varying the cooling rate within the temperature range of 900 °C to 500°C, we identify four distinct microstructures: uniformly distributed fine congruent α_c plates and fine α precipitates, heterogeneous and hierarchical α precipitates, and uniformly distributed coarse α precipitates. Further analysis reveals that these diverse precipitate microstructures originate from three distinct phase transition mechanisms, i.e., congruent transition, pseudospinodal decomposition, and classical nucleation and growth, each activated at different temperatures during continuous cooling. Utilizing the insights from the simulations, we successfully produce microstructures in Ti-5Al-5Mo-5V-3Cr-1Zr (Ti55531) with heterogeneous α precipitates by applying intermediate cooling rates (~0.01°C/s), which activate classical nucleation and growth as well as pseudospinodal decomposition. These samples exhibit exceptional comprehensive mechanical properties, including an ultimate strength of approximately 1260 MPa and a total elongation of around 14 %. This investigation provides valuable guidance for designing novel heterogeneous precipitate microstructures by simply controlling the cooling rate, leading to significant enhancements in the mechanical properties of β-Ti alloys.

1. Introduction

As a vital structural material, titanium (Ti) alloys have been widely used in different fields, such as aerospace [1], orthopedic implants [2], auto industry [3,4] due to their high specific strength [5], good biocompatibility [6,7] and excellent corrosion resistance [8]. The mechanical properties of Ti alloys are mainly determined by the microstructure features such as the morphology, size, distribution, and volume fraction of the HCP (hexagonal close-packed) α precipitate phase [9] in the BCC (body-centered cubic) β phase, which can be modified by different heat treatments (solution treatment, aging, and thermo-mechanical processing) [10]. Aging at temperatures within the α+β two-phase region on the phase diagram after solution treatment is commonly used in industry to increase the strength of β-Ti alloys by inducing α precipitation [11]. Two different precipitation behaviors have been observed in β-Ti alloys by changing the aging temperatures, i.e., conventional nucleation and growth [12] and pseudospinodal decomposition [13–15], which have a significant influence on the size and density of α precipitates [14,16], as well as the corresponding mechanical properties [17,18]. Uniform and fine precipitate

* Corresponding authors.
E-mail addresses: wang_dong1223@xjtu.edu.cn (D. Wang), Yufeng.Zheng@unt.edu (Y. Zheng), wang.363@osu.edu (Y. Wang).

https://doi.org/10.1016/j.actamat.2024.119810
Received 5 December 2023; Received in revised form 19 February 2024; Accepted 1 March 2024
Available online 2 March 2024

microstructures (UM) designed by conventional aging could increase the strength but sacrifice the ductility [19], which are unable to circumvent the longstanding challenge of the strength-ductility trade-off [19–22].

Recent studies have shown that Ti-alloys with a heterogeneous precipitate microstructure (HM) can result in simultaneous improvements in both strength and ductility. [23–36]. A typical HM is known as bimodal microstructure (BM) which consists of micron-sized primary globular α and nanoscale acicular secondary α. These microstructures have been successfully produced via thermomechanical processing and heat treatment [30–36]. Zhu et al. have used β forging plus β transus forging to generate a more complex HM with elongated primary α-phase, sub-micro α-rods, and nanoscale α platelets in Ti-5Al-4Zr-8Mo-7 V, achieving an excellent combination of strength and ductility [26]. However, these traditional methods of designing HM can be complex and costly due to the thermomechanical treatment involved. Concentration modulations have been used to design HM with attractive mechanical properties, including strength and uniform elongation in Ti64+316 L steel [24] and Ti64+Ti5553 [25] hybridized composites. However, these approaches involve alloys with heterogeneous compositions, making them unsuitable for obtaining HM in Ti-alloys with homogeneous compositions. Thus, there is a need for simpler and more effective approaches to designing HM in alloys with homogeneous compositions.

Cooling is an integral part of any heat treatment, which could have a significant impact on the final microstructure and mechanical properties [37–49]. Extensive studies have been done to investigate the relationship between the cooling rate and microstructure in Ti-alloys [40–44]. In Ti64, varying cooling rates from 525°C s^{-1} to 1.5 °C s^{-1} resulted in drastically different microstructures due to the involvement of different types of phase transformations including martensitic, massive, and diffusional phase transformations, which lead to acicular α' martensite, α massive phase, and α Widmanstatten plates, respectively [40]. The volume fraction of α massive phase increased gradually with increasing cooling rate but decreased with further cooling as the martensitic transformation became more favorable [43]. The size of α Widmanstatten plates increased with decreasing cooling rate [41], accompanied by decreasing tensile strength and increasing ductility. Thus, these UMs produced by cooling do not resolve the trade-off between strength and ductility. The sensitivity of various phase transformation mechanisms to cooling rates presents promising opportunities for designing heterogeneous microstructures (HMs). By precisely adjusting the cooling rate, different phase transformation mechanisms can be selectively activated at specific temperatures and durations, allowing for precise tailoring of the HM design.

The occurrence of bimodal or even trimodal heterogeneous microstructures (HMs) has been observed in Ni-based superalloys during continuous cooling. These findings provide valuable insights and serve as a positive inspiration for the formation of HMs in Ti alloys through the regulation of cooling rates [50–52]. For instance, Badu et al. conducted a study where they demonstrated the presence of fine secondary γ' precipitates (~20 nm) alongside the coarse primary γ' precipitates under intermediate cooling conditions of 1 K/s [50]. The formation of a bimodal size distribution of γ' can be attributed to the competitive interplay between nucleation events and atomic diffusion under intermediate cooling rates [52].

The purpose of this study is to investigate the potential for producing heterogeneous microstructures (HMs) by controlling the cooling rate through a combination of computational simulations and experimental methods. Using near-β Ti alloys as a case study, we initially establish a close correlation between the cooling rate and microstructure by precisely controlling the cooling rate using phase field simulations. Leveraging the extensive simulation data, we subsequently construct a continuous cooling diagram for the Ti-Mo system to screen for optimal microstructures. Undoubtedly, the HM corresponding to the intermediate cooling rate emerges as a promising approach for enhancing the alloy's performance. Guided by the simulation results, we successfully design an HM in Ti55531, leading to a synergistic improvement in both strength and ductility. Furthermore, we investigate the underlying transition mechanisms responsible for the formation of different microstructures at varying cooling rates. The generation of the HM is found to result from a combination of classical nucleation and growth mechanisms, along with pseudospinodal decomposition.

2. Method

2.1. Phase field model

Since phase field simulations will be used as a semi-quantitative guide to the experiment, we consider pseudobinary systems with Mo elements for simplicity. Ti-8.15Mo with the exact β-equivalent stabilizing element Mo (i.e., the Mo-equivalency) is selected to represent Ti55531 in the experiments [53]. The chemical free energy curves of the α and β phases and their intersection point c_0 at different temperatures, obtained from the Pandat thermodynamic database, are shown in Fig. 1. Fig. 1(a) shows the temperature dependence of the free energy curves of α and β phases and Fig. 1(b) shows the free energy surfaces as functions of both concentration and structural order parameter at 650°C. Fig. 1(c) shows the temperature dependence of c_0 for Ti-Mo, and Fig. 1(d) shows the interdiffusion coefficient $D_{Ti-Mo}(T)$ as a function of temperature [54–56].

Considering a two-dimensional computational cell with 512 × 512 numerical grids on a $(11\bar{1})$ the plane, three equivalent α variants by 120° rotation have been used in our simulations, and the stress-free transformation strain can be calculated based on Burgers orientation and lattice constant a_β=3.254Å, a_α=2.945Å, c_α=4.674Å [57].

$$\varepsilon_1 = \begin{pmatrix} 3.50\% & 0 & 0 \\ 0 & -2.33\% & 9.39\% \\ 0 & 9.39\% & 6.33\% \end{pmatrix}$$

$$\varepsilon_2 = \begin{pmatrix} -8.71\% & -2.52\% & -8.14\% \\ -2.52\% & 0.204\% & -4.70\% \\ -8.14\% & -4.70\% & 6.33\% \end{pmatrix}$$

$$\varepsilon_3 = \begin{pmatrix} -8.71\% & 2.52\% & 8.14\% \\ 2.52\% & 0.204\% & -4.70\% \\ 8.14\% & -4.70\% & 6.33\% \end{pmatrix}$$

The total free energy can be represented by conserved concentration field (c) and non-conserved structure order parameter field (η) [15,23,27]:

$$\begin{aligned} F = & \int_V \left[\sum_p h(\eta_P) g_\alpha(c_{Mo}, T) + \left(1 - \sum_P h(\eta_P)\right) g_\beta(c_{Mo}, T) \right. \\ & \left. + \omega_1 \sum_P \sum_{p \neq q} \eta_P \eta_q + \sum_p \omega_2 \left(\eta_P^2 - 2\eta_P^3 + \eta_P^4\right) + \frac{k}{2} (\nabla c_{Mo})^2 + \frac{\varepsilon}{2} \sum_P (\nabla \eta_P)^2 + E^{elastic} \right] \end{aligned} \quad (1)$$

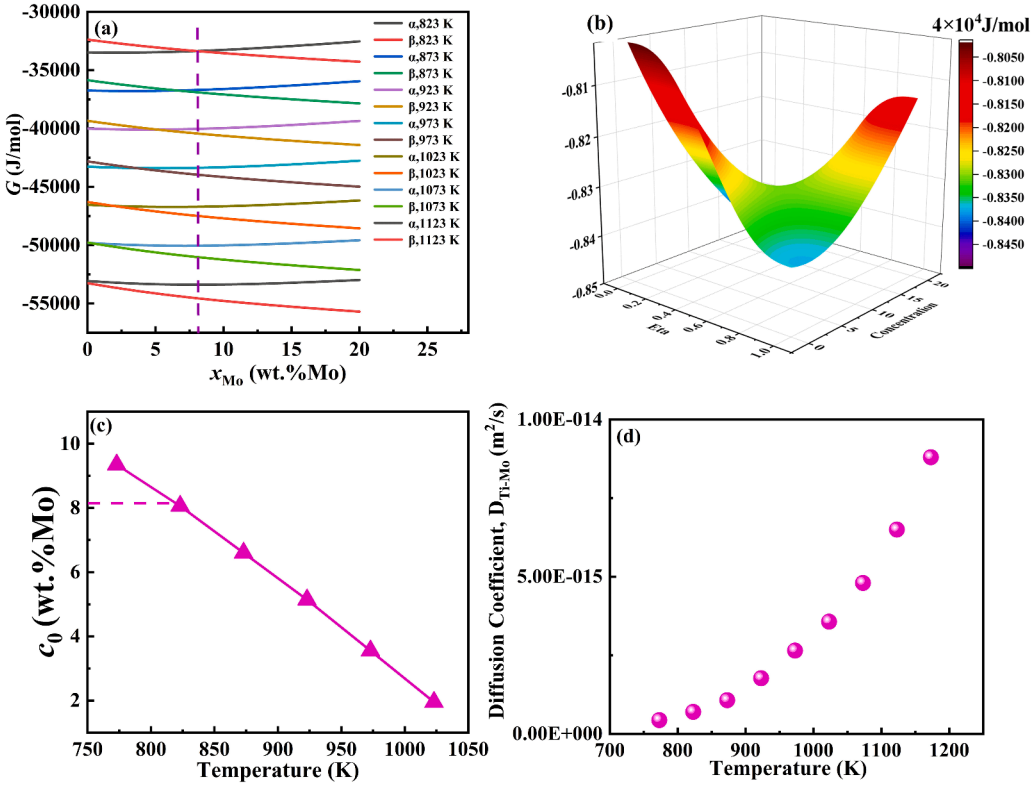

Fig. 1. Thermodynamic data for Ti-Mo systems. (a) The chemical free energy vs. composition curves for the α and β phases in the Ti-Mo system at various temperatures. (b) The chemical free energy surfaces in the composition and structural order parameter space for the Ti-Mo system at 650°C. (c) The value of c_0, representing the composition at which the two free energy curves intersect, for various Ti-Mo binary alloys at different temperatures. (d) The interdiffusion coefficient in Ti-Mo system at different temperatures.

Where η_p represents the structural order parameter of the p^{th} α variants, and c_{Mo} represents the concentration of molybdenum. ε and κ are the gradient energy coefficients of the structural field and concentration field. w_1 and w_2 stand for the energy barrier between the α phase and β phase and among different α variants, respectively [23]. $g_\alpha(c_{Mo}, T)$ and $g_\beta(c_{Mo}, T)$ describe the chemical free energy of α and β phases from the Pandat database, which is related to composition and temperature, and fitted by polynomial functions as follows:

$$\begin{aligned} g_\alpha &= (-65.3T + 2441.3) \\ &+(-21.7T + 10215.0)c_{Mo} + (42.9T + 14330.9)c_{Mo}^2 + (132.9T + 32437.3)_{Mo}^3 \\ &+(-1774.3T - 474017.2)c_{Mo}^4 + (7094.1T + 1.89423E6)c_{Mo}^5 + (-14595.2T - 3.9081E6)c_{Mo}^6 \\ &+(16670.9T + 4.46238E6)c_{Mo}^7 + (-10030.8T - 2.68377E6)c_{Mo}^8 + (2486.5T + 663278.4)c_{Mo}^9 \end{aligned} \quad (2)$$

$$\begin{aligned} g_\beta &= (-69.6T + 5897.1) \\ &+(-16.5T - 5970.2)c_{Mo} + (43.7T + 9480.6)c_{Mo}^2 + (134.6T + 32922.9)c_{Mo}^3 \\ &+(-1782.4T - 479852.8)c_{Mo}^4 + (7110.9T + 1.92454E6)c_{Mo}^5 + (-14618.1T - 3.97253E6)c_{Mo}^6 \\ &+(16687.0T + 4.54777E6)c_{Mo}^7 + (-10036.2T - 2.74241E6)c_{Mo}^8 + (2486.6T + 681652.6)c_{Mo}^9 \end{aligned} \quad (3)$$

The interpolation function is described by $h(\eta_i)$ as follows [15]:

$$h(\eta) = \eta^3(6\eta^2 - 15\eta + 10) \quad (4)$$

which allows the free energy curves to connect smoothly with the function of individual concentrations in the dimension of the structural order parameter. The non-equilibrium total free energy $G(c, \eta)$ is now a hypersurface as functions of η and concentration c, as shown in Fig. 1b. This simple interpolation function, h, is usually used to connect the two equilibrium free energy curves in phase field simulation [23]. When the total free energy is minimized concerning the structural order parameter, η, two solutions can be obtained. One is $\eta = 0$, corresponding to the equilibrium free energy curve of β phase, G_β, and the other is $\eta = 1$, corresponding to the equilibrium free energy curve of α phase, G_α.

The temperature range for cooling used in our simulations is between 900°C (higher than the β-transus temperature 850°C) and 500°C to avoid the brittle ω phase at a lower temperature. The value of c_0 (the intersection of the free energy curves of α phase and β phase) of different systems decreases linearly as the temperature increases, as shown in Fig. 1c.

Based on the Khachaturyan-Shatalov theory, the contribution of elastic interaction energy can be derived as follows [15,23,27,58]:

$$E^{\text{elastic}} = \frac{1}{2}\int_V \frac{d\vec{k}}{2\pi^3}\sum_{p,q}^{3} B_{pq}(\vec{n})\tilde{\eta}_p\left(\vec{k}\right)\tilde{\eta}_q^*\left(\vec{k}\right) \quad (5)$$

Where $\vec{n}$ is a unit vector, $B_{pq}(\vec{n})$ is the transformation strain function for each α variant [15,23,27,58]:

$$B_{pq}(\vec{n}) = C_{ijkl}\varepsilon_{ij}^{\mathrm{T}}(p)\varepsilon_{kl}^{\mathrm{T}}(q) - \vec{n}_i\sigma_{ij}^{\mathrm{T}}(p)\Omega_{jk}(\vec{n})\sigma_{kl}^{\mathrm{T}}(q)\vec{n}_l \quad (6)$$

In which C_{ijkl} is the stiffness tensor, $\varepsilon_{ij}^{\mathrm{T}}(p)$ is the stress-free transformation strain of the p^{th} variant, and $\sigma_{ij}^{\mathrm{T}}(p) = C_{ijkl}\varepsilon_{kl}^{\mathrm{T}}$, $[\Omega(\vec{n})]_{ik}^{-1} = C_{ijkl}n_jn_l[\Omega(\vec{n})]$. Our work focuses on the early stage of α nucleation, where coherent boundary assumption is used in our simulations.

The microstructural evolution for the concentration field and structure field can be obtained by solving the Chan-Hilliard (CH) equation and Time-Dependent Ginzburg-Landau (TDGL) equation, respectively [15,23,27,58–60].

$$\frac{\partial c_{\mathrm{Mo}}}{\partial t} = \nabla\left(M_{\mathrm{Ti-Mo}}(T)\nabla\frac{\delta F}{\delta c_{\mathrm{Mo}}}\right) + \xi_c(T) \quad (7)$$

$$\frac{\partial \eta_p}{\partial t} = -L\frac{\delta F}{\delta \eta_p} + \xi_\eta(T) \quad (8)$$

Where $M_{\mathrm{Ti-Mo}}(T)$ stands for chemical mobility. According to Andersson and Agren [61], chemical mobility is related to atomic mobility $M_{\mathrm{Ti-Mo}}^0(T)$: $M_{\mathrm{Ti-Mo}}(T) = c_{\mathrm{Mo}}(1-c_{\mathrm{Mo}})M_{\mathrm{Ti-Mo}}^0(T)$ [52,62,63], which is associated with the temperature-dependent interdiffusion coefficient $D_{\mathrm{Ti-Mo}}(T)$ shown in Fig. 1(d) through $M_{\mathrm{Ti-Mo}}^0(T) = D_{\mathrm{Ti-Mo}}(T)/RT$ [52,62], R is the gas constant, and T is the absolute temperature. The coefficient $c_{\mathrm{Mo}}(1\text{-}c_{\mathrm{Mo}})$ has been included to ensure that the diffusion equation for the solute has a diffusion coefficient dependent on the alloy's local concentration [52]. L represents the structural mobility of the structural field, which is assumed temperature independence. ξ_c and $\xi\eta$ stand for the Langevin force terms of the concentration field and structural field to simulate thermal fluctuation closely related to temperature [15,23,27,58–60].

$$\xi_\eta = (n,m) = \sqrt{2k_BTL/(\lambda^d\Delta t)\rho} \quad (9)$$

$$\xi_c = (n,m) = \sqrt{2k_BTM/(\lambda^d\Delta t)\nabla\cdot\rho} \quad (10)$$

The elastic constants can be obtained from the experimental measurements: C_{11}=160.5 GPa, C_{12}=125.6 GPa, and C_{44}=34.1 GPa [27]. The coherent interfacial energy between the two phases is assumed to be 100 mJ/m^2 [27]. The normalizing factor E_{norm}=40 KJ/mol is used for dimensionless forms to solve kinetic equations. The dimensionless mobility parameters which assure the diffusion-controlled growth process are assumed to be temperature-independent structural evolution coefficient L = 20, The atomic mobility $M_{\mathrm{Ti-Mo}}^0(T)$ (nm^2/J·s) for the Ti-Mo system is $M_{\mathrm{Ti-Mo}}^0(T) = (3.48E5/T)\exp(-6843.65/T)$, and the diffusion coefficient $D_{\mathrm{Ti-Mo}}(T)$ (m^2/s) is $D_{\mathrm{Ti-Mo}}(T) = (2.89\mathrm{E}-12)\exp(-$

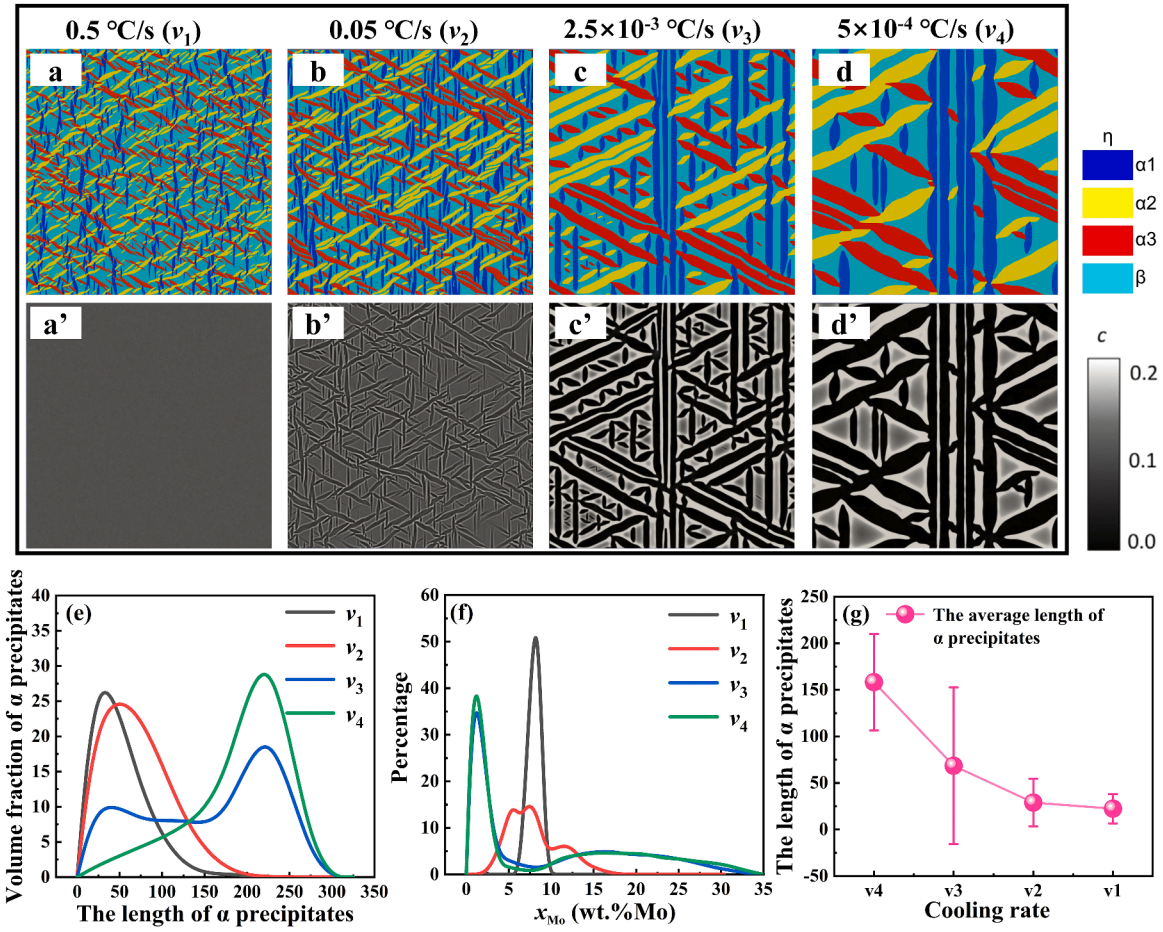

Fig. 2. Calculated morphology of α precipitates along with the statistical results of length and concentration distributions following different cooling rates. (a)-(d) The corresponding structural order parameter fields after different cooling rates. Light blue represents the β phase, and dark blue, yellow, and red describe three variants of the α precipitates. (a')-(d') The composition fields after different cooling rates, black color, and gray color stand for the α phase and β phase, respectively. (e) The relationship between length and volume fraction of α precipitates after different cooling rates. (f) The statistical distribution of concentration after different cooling rates. (g) The average length and error distribution of α precipitates after different cooling rates.

6843.65 /T)[55]. The dimensionless energy barrier coefficient between different α variants and α phase and β phase are w_1*=0.06, and w_2*=0.01, respectively. The dimensionless gradient energy coefficients are κ_η* = 0.01, κ_c*= 1.2, which, combined with the selected interface energy, produces a dimensional grid size of ~10 nm. The dimensionless time step $\Delta t^* = 0.01$, combined with $M^0_{\mathrm{Ti-Mo}}(T)$grid size and CH equation, can be converted to real-time step $\Delta t = 0.01$ s.

The cooling rate is described through $\Delta T/t$ by changing the value of t for the same temperature range (from 900°C to 500°C to avoid the possible brittle ω phase). With the assistance of phase field simulations, the microstructure evolution of β-Ti alloys under different cooling rates (e.g., v_1: 0.5°C/s, v_2: 0.05°C/s, v_3: 2.5 × 10^{-3}°C/s, v_4: 5.0 × 10^{-4}°C/s and so on) are studied.

2.2. Experimental method

The commercial Ti55531 (Ti-5.2Al-4.79Mo-4.83V-2.77Cr-1.07Zr-0.35Fe (wt.%)) alloy with $T_\beta \sim 835 \pm 5$ is acquired from Northwest Institute for Nonferrous Metal Research, China. The specimens are cut into cylindrical rods 13 mm diameter × 10 mm by a wire cutting machine. These specimens are first heat-treated at 850°C for 1 h, followed by cooling treatments at different rates (0.05°C/s, 0.01°C/s, 0.0025°C/s, and 0.001°C/s) until reaching a temperature of 500°C and then water quenched to room temperature. Different cooling rates are determined by setting the furnace subsystem's initial temperature, cooling time, and end temperature. After that, the specimens are etched in a solution mixture of 2: 8: 90 of HF, HNO3, and H2O in volume fraction for microstructure observation using SU-6600 scanning electron microscope (SEM), and the quantitative statistics of SEM images are completed by Image-Pro-Plus. Cylindrical tensile specimens with 6 mm diameter × 30 mm gage length (ASTM E8) are subsequently machined to conduct the stress-strain tensile test with INSTRON 1195 test machine at a constant strain rate of 5.6 × 10^{-4} s^{-1}.

3. Results

3.1. Microstructural evolution under different cooling rates

Microstructures obtained from the phase field simulations under different cooling rates from 900°C to 500°C are shown in Fig. 2, which are quite different in terms of α precipitate size, shape, aspect ratio, and spatial distribution of different variants. As the decrease of the cooling rate, the microstructure goes through four different conditions, i.e., congruent β (bcc) - α (hcp, will be referred to as α_c hereafter) structure transformation without composition change (Fig. 2a), UM with fine α precipitates (Fig. 2b), HM with clear hierarchical α precipitates (Fig. 2c), and UM with coarse α precipitates. Upon fast cooling v_1 (0.5 °C/s), a large number of fine acicular α_c precipitates (Fig. 2a) are generated from the structural transformation, but the concentration does not show any inhomogeneity (Fig. 2a'). To avoid the formation of ω phase in Ti-alloys during rapid cooling [46,64], the end temperature is set to 500°C. For the slower cooling rates (i.e., the last three columns in Fig. 2), the structural transformation and solute partitioning occurs simultaneously. It should be noted that grain boundaries or other defects are not considered in our simulations, which may also influence the microstructures.

The statistical analysis of the α precipitate microstructure obtained under different cooling rates is shown in Fig. 2(e) and (f). Fig 2(e) illustrates the volume fractions of α precipitates categorized by their lengths, showing a shift in size distribution as the cooling rate decreases from v_1 to v_2. The α precipitate sizes exhibit a unimodal distribution that becomes broader and shifts towards larger sizes. Notably, an evident

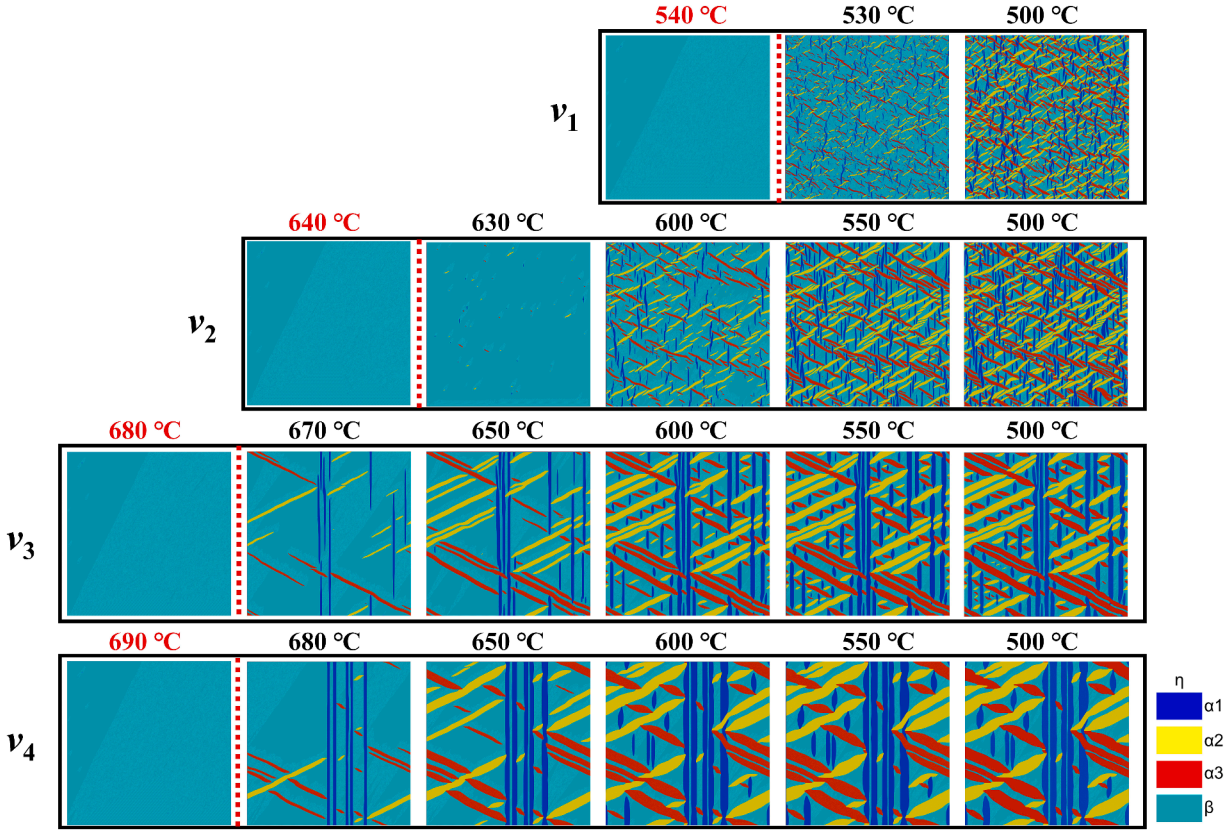

Fig. 3. The microstructural evolution for the formation of α precipitate at different temperatures under different cooling rates. Light blue represents the beta phase, and dark blue, yellow, and red represent three alpha variants. The critical transition temperature, T_s, (the temperature at which α precipitates begin to appear under cooling) is marked by red color.

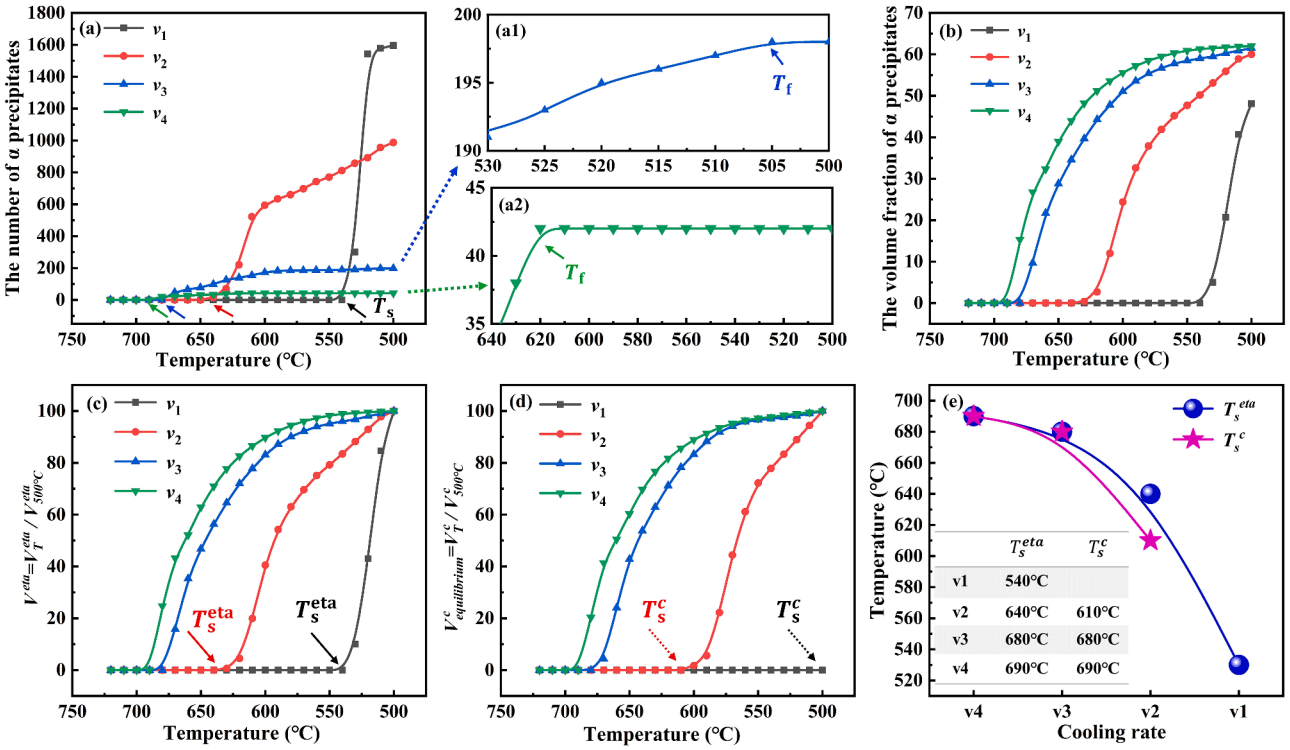

Fig. 4. The statistical results of the simulation results. (a) The number density of α precipitates with decreasing temperature at different cooling rates. (a1) and (a2) Local magnifications of the v_3 and v_4 curves in Fig. 4(a). (b) The volume fraction of α precipitates with decreasing temperature at different cooling rates. (c) The normalized percentage of α precipitates the volume of the structure field (η=1). (d) The normalized percentage of α precipitates volume of concentration field (c = 2%). (e) The transition start temperature for the structural field and concentration field of different cooling rates. The inset table compares the critical transition temperature of the structural field and concentration field at different cooling rates.

bimodal size distribution emerges under the cooling rate v_3. As the cooling rate further decreases to v_4, the average length of the α precipitates increases, resulting in a sharp unimodal distribution within a larger size range. The concentration in Fig. 2(f) reveals that under cooling rate v_1, the concentration exhibits a unimodal distribution centered around an initial concentration of approximately 8.15 wt.%, indicating a congruent transition. As the cooling rate decreases to v_2, the concentration distribution broadens, spanning between the equilibrium concentration of the α phase (~2 wt.%) and the β matrix. With further decreases in the cooling rate (v_3 and v_4), the concentration distribution demonstrates a distinct bimodal pattern, characterized by the equilibrium concentration of the α phase (~2 wt.%) and a broad concentration distribution within the β matrix. Fig. 2(g) depicts the gradual increase in the average length of α precipitates along with a varying width of the size distribution as the cooling rate decreases. Initially, the width of the size distribution increases, followed by a subsequent decrease.

The microstructures obtained at different temperatures under a given cooling rate are shown in Fig. 3. The results indicate that no α precipitation above 700°C under these cooling conditions (v_1-v_4) and it is the cooling within a relatively narrow temperature window between 700°C and 500°C that determines the microstructure development. With the decrease in cooling rate, the transformation start temperature, T_s, (i.e., the temperature at which α precipitates begin to appear) increases.

Fig. 4(a) shows the number density of α precipitates (number of precipitates within the computational cell) as a function of temperature. The critical transition temperature (T_s) and nucleation finish temperature (T_f) have been determined through statistical analysis of the number density presented in Fig. 4 of the revised manuscript. The temperature interval, currently set at 10°C, may affect the precision of these values (±5°C), yet the overall trend is expected to be accurate. In addition, the nucleation process is governed by Langevin noise in our phase field simulations. If the number of nucleation is high with a rapid cooling rate, the statistical outcomes are considered reliable. However, if the nucleation count is low with a slow cooling rate, additional simulations are likely required. Additionally, for the convenience of calculating the number density of fine α/α_c precipitates generated under v_1/v_2 within the error range, we ignored the influence of Fourier-boundary condition. There is a sudden increase in the number density of α precipitates at fast cooling rates (v_1 or v_2), and the final number density of α precipitates at 500°C decreases with decreasing cooling rate. In addition, the critical transition temperature T_s marked with arrows increases with decreasing cooling rate. Fig. 4(a1) and (a2) provide local magnifications of the v_3 and v_4 curves in Fig. 4(a). Observing these two cooling rates, it becomes apparent that the number density of α precipitates does not exhibit a continuous increase as the temperature decreases. In this context, we define the nucleation and growth finished temperature (T_f) as the temperature that marks the conclusion of α precipitation during the cooling process. Fig. 4(b) shows the volume fraction of α precipitates at different temperatures upon cooling under different rates. To identify the transformation start temperatures, we plot the normalized volume fractions of α_c and α phases calculated by the volume fraction at 500°C through the structural order parameter field (when η=1, ie., HCP strucuture), i.e., $V_0^{\eta} = \frac{V_T^{\eta}}{V_{500°C}^{\eta}}$, and through the concentration field (when c = 2.0 wt.% i.e., the equilibrium concentration of α phases), $V_0^{c} = \frac{V_T^{c}}{V_{500°C}^{c}}$, at different cooling rates in Fig. 4(c) and (d), respectively. The transformation start temperatures determined (see the solid and dotted arrows in Fig. 4(c) and (d)) are plotted in Fig. 4(e), where T_s^{η} and T_s^{c} coincide with each other at slow cooling rates and start to deviate from each other at fast cooling rates, which suggests the activation of congruent and pseudospinodal decomposition transformation processes. Besides, both transformations start temperatures are inversely proportional to the cooling rate.

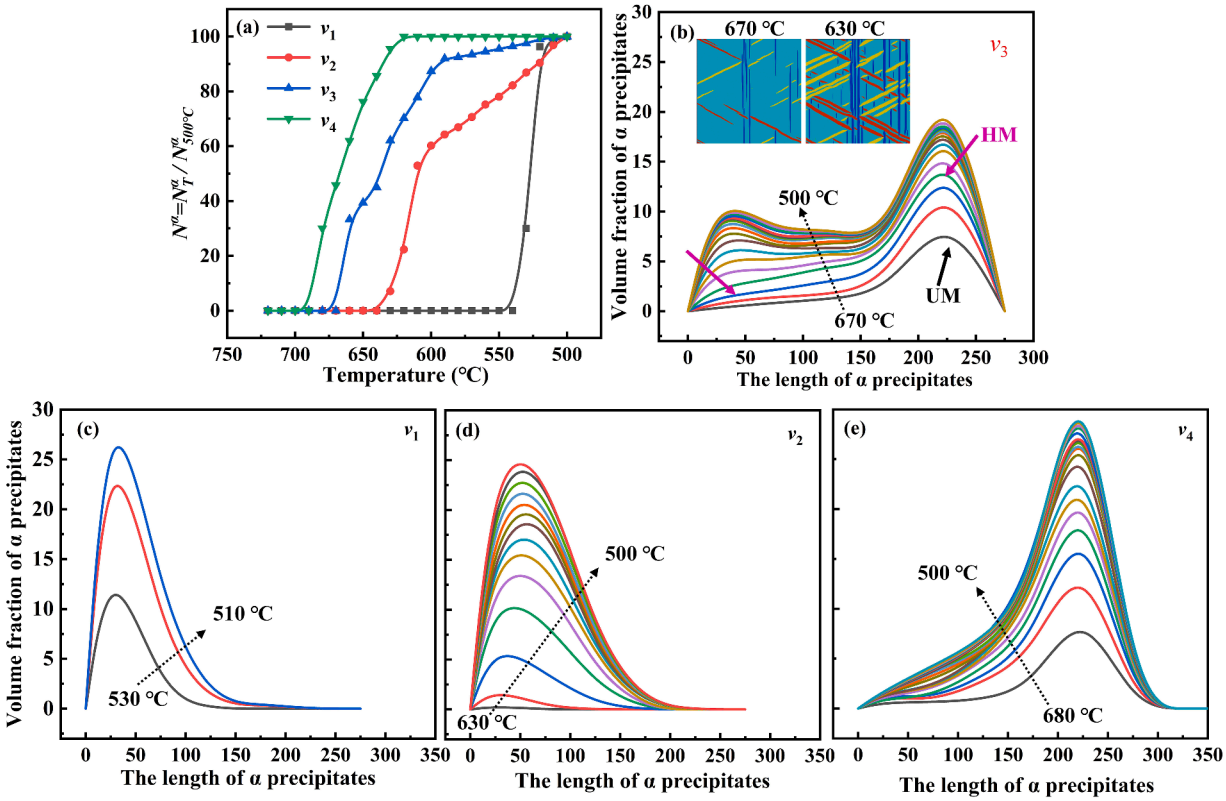

Fig. 5. The statistical results of the simulation results. (a) The normalized number density of α precipitates at different temperatures for different cooling rates. (b), (c), (d), and (e) The relationship between length and volume fraction of α precipitates to varying temperatures for cooling v_3, v_1, v_2, and v_4, respectively.

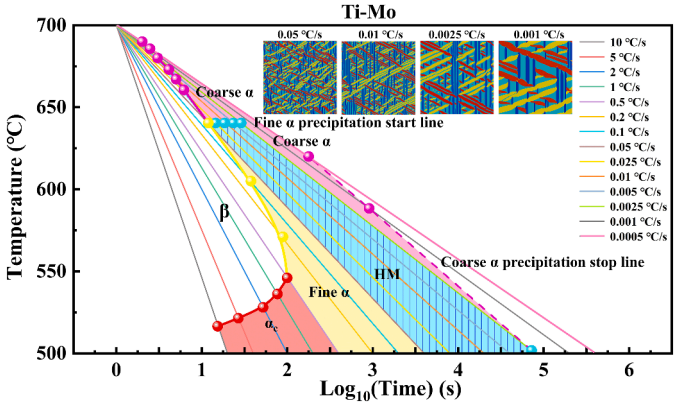

Fig. 6. The diagram under continuous cooling (from 0.0005 to 10°C/s) for different microstructure. Red region represents the α_c due to congruent transition, yellow region represents the fine α due to pseudospinodal decomposition, blue region represents the heterogeneous microstructure (HM), pink region represents the coarse α due to classical nucleation and growth. Blue line describes the fine α precipitate nucleation start line and pink solid line describes the coarse α precipitate nucleation start line.

3.2. Multi-scale α HM for intermediate cooling rate

The size distributions in Fig. 2 indicate the existence of bimodal distribution at the intermediate cooling rate v_3. The detailed number density and size distributions at different temperatures for cooling rate v_3 have been calculated and plotted in Fig. 5. Fig. 5(a) shows the normalized number density of α precipitates calculated by using the structural order parameter field, $N^{\eta}_0 = \frac{N^{\eta}_T}{N^{\eta}_{500°C}}$, at different temperatures under different cooling rates. Under cooling rate v_3, a two-step transformation behavior characterized by two transformations start temperatures at $T^{\eta}_{s1} = 680°C$ and $T^{\eta}_{s2} = 640°C$ can be observed. The size distribution of α precipitates at different temperatures under cooling rate v_3 varies from a uniform distribution to a bimodal distribution as shown in Fig. 5(b), which is in sharp contrast to those obtained under other cooling rates (v_1, v_2, v_4) where only a single-peak exists at different temperatures.

According to the transformation start temperatures obtained and the nucleation and growth finished temperatures under different cooling rates, the diagram under continuous cooling can be drawn, as shown in Fig. 6. Overall, ultrafine congruent α_c (red shadow), fine α (yellow shadow), and coarse α (pink shadow) will be produced from fast to slow cooling. Under the intermediate cooling rate, a particular HM region (blue shadow) consisting of coarse α and fine α appears. The appearance of the HM region is consistent with the two-step phase transformation characteristics shown in Fig. 5: the appearance of high temperature T^{η}_{s1} leads to the formation of a coarse α (pink shadow), followed by the appearance of T^{η}_{s2}, at which fine α precipitates start to form. T^{η}_{s1} increases with decreasing cooling rate while T^{η}_{s2} remaining constant at 640°C. When fine α is completely suppressed, the coarse α precipitation stop line appears simultaneously, and the system transfer from the HM region to the coarse α region (pink shadow). Thus, for the Ti-Mo system, the intermediate cooling rates offer the opportunity to achieve HMs by continuous cooling.

3.3. Experimental design of HM for Ti55531

Based on the simulation results and continuous cooling diagram, four cooling rates are designed experimentally for a commercial alloy Ti55531 to achieve UMs with fine and coarse α precipitates and HMs with multi-scale α precipitates. It should be noted that due to our experimental equipment being unable to accurately control the super-fast cooling rate, the simulation results for ultrafine α_c region have not

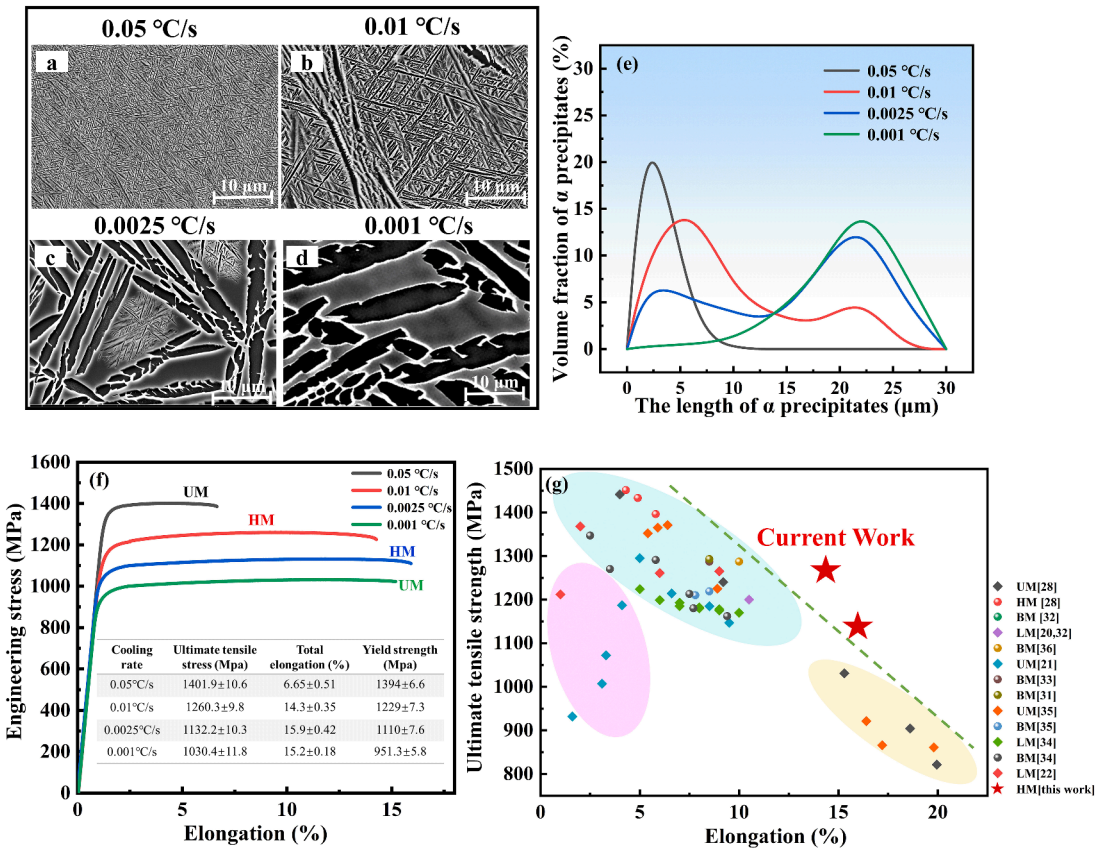

Fig. 7. Typical experimental results and mechanical properties of model materials Ti55531 samples after different cooling rates. (a) SEM micrograph for the UM with fine α precipitates under cooling rate 0.05°C/s (b)-(c) SEM micrograph for the HM with a mixture of fine α precipitates and coarse α precipitates under cooling rate 0.01°C/s and 0.0025°C/s, respectively. (d) SEM micrograph for the UM with coarse α precipitates under cooling rate 0.001°C/s (e) The relationship between the length and volume fraction of α precipitates corresponding to SEM micrographs. (f) Stress-strain curves for different cooling rates. (g) Ultimate tensile strength versus elongation of Ti55531 alloys under different heat treatments [20–22,28,29,31–36].

been validated by relevant experiment. Fig. 7(a) shows a UM with fine α precipitates under a fast cooling rate which shows high strength but low ductility (Fig. 7(f)), contrary to the mechanical properties of the UM with coarse α precipitates (Fig. 7(d) and (f)). The α lath length distribution of these two UMs is unimodal, as shown in Fig. 7(e). The average size of α in the UM corresponding to Fig. 7(a) and Fig. 7(d) is 3 μm and 23 μm, respectively. Fig. 7(b)-(c) display two typical HMs under two intermediate cooling rates 0.01°C/s and 0.0025°C/s. In the former (Fig 7 (b)) coarse α precipitates are surrounded by fine α precipitates, while in the latter (Fig. 7(c)) fine α precipitates are surrounded by coarse α precipitates. As shown in Fig. 7(e), the α lath length distribution of these HMs has bimodal feature, where the average length of fine α precipitates and coarse α precipitates is around 5 μm and 23 μm, respectively. Besides, with the decrease of cooling rate, the bimodal distribution changes from a larger percentage of fine α precipitates to a larger percentage of coarse α precipitates. Fig. 7(f) compares the stress-strain curves and related mechanical properties of several microstructures shown in Fig. 7 (a)-(d). The strength of UM with fine α precipitates is as high as ~1400 MPa, but at the cost of strong ductility sacrifice (~6.7 %), while the strength of UM with coarse α precipitates has the lowest strength (~1030 MPa) under the condition of ensuring ductility (~15.2 %). HMs inherit the performance advantages of the above two types of UMs. Compared with UM with coarse α precipitates, the strength (~1132 MPa) and ductility (~15.9 %) of HM generated by 0.0025°C/s increase simultaneously. With the increase of the volume fraction of fine α precipitates, the strength (~1260 MPa) of HM generated by 0.01°C/s is further improved with the slight reduction of ductility (~14 %). Abundant fine α precipitates in HM are instrumental in resisting short-range crack propagation and dislocation movement and avoiding local stress/strain concentration [27,28]. At the same time, the small number of coarse α precipitates may delay crack initiation by triggering the deformation twin [27,29] to coordinate deformation, and they are beneficial to break the continuity of cross-high-strain bands to resist long-range crack growth [27]. The relationships between total elongation and ultimate strength of Ti53331 under different heat treatments [20–22,28,29,31–36] are summarized in Fig. 7(g), which indicates the comprehensive mechanical properties of hierarchical HMs are further enhanced. Under the 0.01°C/s cooling rate, the strength of the HMs is as high as 1260 MPa, accompanied by a high ductility up to 14%. Compared with the traditional bimodal microstructure with primary α and secondary fine α, the ductility of HM is improved with an almost constant strength. The experimental work corresponds well with the simulation results, demonstrating that our simulation model is helpful for predicting microstructure evolution and guiding the experimental design of HMs.

4. Discussion

4.1. Transformation mechanisms for the formation of hm

Different microstructures developed under different cooling rates can be attributed to different transformation mechanisms activated along the cooling paths. According to the free energy curves of the α and β phases (Fig. 1(a)), congruent β → α transformation takes place at low β-stabilizer content, pseudospinodal decomposition mechanism takes place at intermediate β stabilizer content, and nucleation and growth mechanism operates at high β stabilizer content [23]. The low, intermediate, are high β stabilizer contents are relative to c_0 at which the two

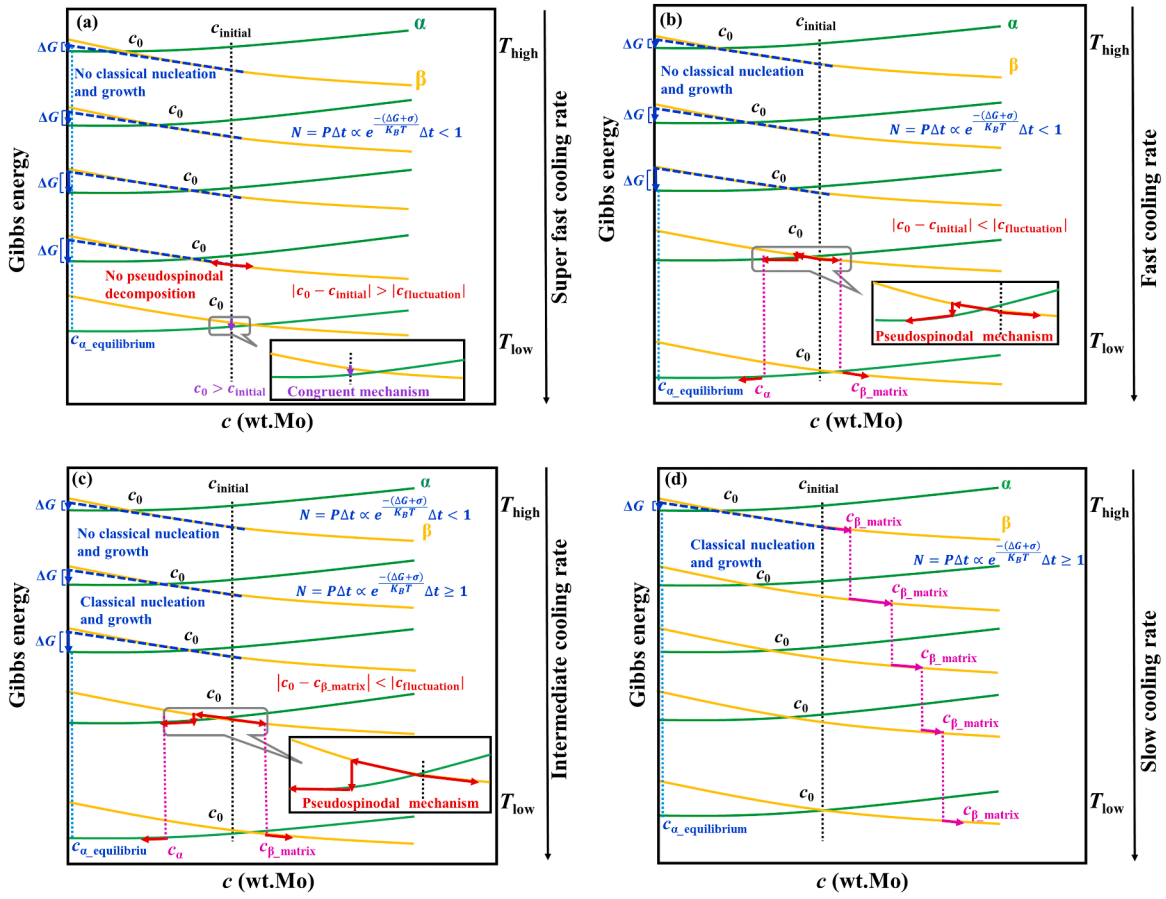

Fig. 8. Schematic drawings of transformation mechanisms activated along the cooling paths at different cooling rates: (a) super-fast, (b) fast, (c) intermediate, and (d) slow. The green and yellow lines represent the free energy curves of the α and β phases, respectively. The black dotted line indicates the starting alloy composition ($c_{initial}$). The pink dotted lines indicate the evolution of the β matrix ($c_{β\_matrix}$) and non-equilibrium α phase ($c_α$) compositions during cooling. The light blue dotted line stands for the equilibrium composition of the α phase ($c_{α\_equlibrium}$). The dark blue dashed lines are tangent lines to the β phase free energy curves at the alloy composition at different temperatures. ΔG is the driving force of the initial phase transition, indicated by the blue arrow that marks the difference between the tangent line and the α free energy curve at its equilibrium composition. The pink arrows point to the evolution of the matrix composition at different temperatures. The red arrows represent the thermal fluctuation and pseudospinodal mechanisms. The purple arrows represent the congruent transformations.

free energy curves intersect. Based on the temperature dependence of c_0 shown in Fig. 1(c), the increase of c_0 with decreasing temperature (950°C-500°C) suggests a possible change in transformation mechanisms upon cooling, e.g., from the classical nucleation and growth mechanism [12,27] to pseudospinodal mechanism [15,27] to congruent transformation mechanism [23,27,28]. In Fig. 8, various transformation mechanisms that could be activated at different cooling rates are illustrated. The number of nuclei can be calculated by $N = P\Delta t \propto e^{\frac{-(\Delta G+\sigma)}{K_B T}} \Delta t$, where P is the nucleation rate, $\Delta t$is the unit time of transformation (time interval spent at each temperature at a given linear cooling rate), $\Delta G$is the driving force for beta to alpha phase transition, σ is the nucleation barrier due to interfacial energy and elastic interaction, T is the temperature and k_B is the Boltzmann constant. When the cooling rate is super-fast (Fig. 8(a)), neither the classical nucleation and growth mechanism nor the pseudospinodal decomposition mechanism could be activated due to a lack of incubation time and time for long and intermediate range diffusion. However, when the temperature continuously decreases, the congruent mechanism, which requires only short-range diffusion, could be activated once c_0 moves to the right of $c_{initial}$. When the cooling rate is decreased (Fig. 8(b)), $c_{initial}$ gradually approaches to c_0 and the time duration when $c_{initial}$ and c_0 are in close proximity is long enough to allow the pseudospinodal decomposition mechanism [15] to take place. At intermediate cooling rates (Fig. 8(c)), nucleation and growth mechanism can be activated at high temperatures when $c_{initial}$ is far away from c_0 and the time duration is long enough for the nucleation to occur. Meanwhile, the untransformed β-phase matrix can still satisfy the condition for activating the pseudospinodal mechanism at lower temperatures. Thus, it is possible to simultaneously activate two mechanisms at an intermediate cooling rate, which is essential for the formation of HMs. As the cooling rate further decreases (Fig. 8(d)), the classical nucleation and growth process activated at higher temperatures would have enough time to proceed and $c_{β\_matrix}$ would be rich to such a degree that the pseudospinodal mechanism can no longer operate anymore and, thus, preventing the formation of HMs.

Fig. 9 shows the concentration distribution with the decrease in temperature along different cooling paths and the free energy curves at critical temperatures. The combination of the classical nucleation mechanism and the pseudospinodal mechanism is the origin of the hierarchical HMs of α precipitates under intermediate cooling rate v_3, as indicated by the two temperature ranges shown in Fig. 5(a). Fig. 9(c) and (c') show that the classical nucleation and growth mechanism occurs at the high temperature (680°C), which also can be inferred from the sudden jump of α phase concentration to its equilibrium concentration. As the temperature decreases to below 640°C, the pseudospinodal mechanism is activated due to sufficient time and the relatively low β stabilizer content ($Dc=c_{β\_matrix} - c_0<2.5\%$ [28]).

For fast cooling rate v_2, the short time span at each temperature suppresses the classical nucleation and growth mechanism in the high temperature range, and coarse α cannot be formed. When the

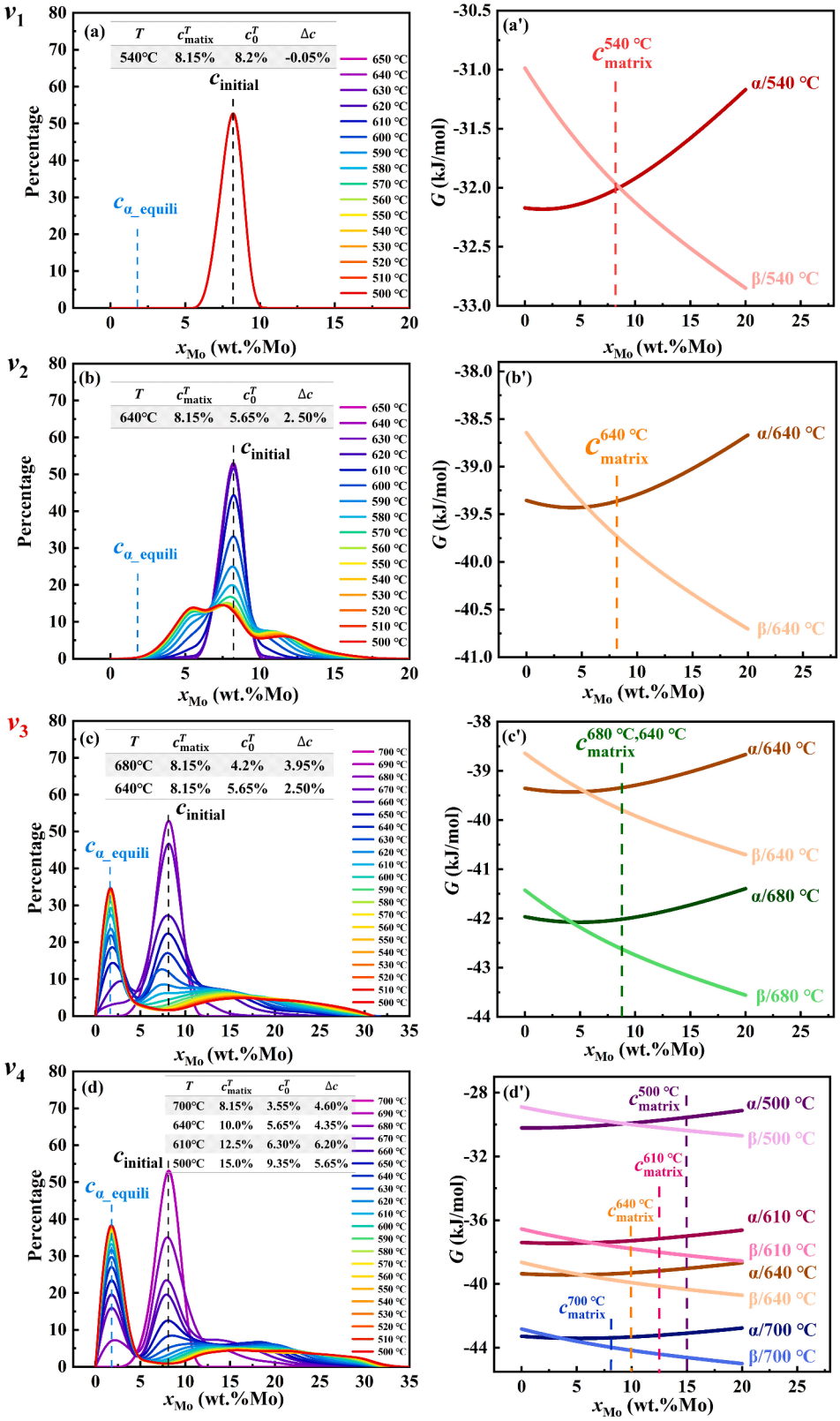

Fig. 9. The statistical distribution of concentration at different temperatures under different cooling rates and free energy curves. (a)-(d) The statistical distribution of concentration at different temperatures under cooling v_1, v_2, v_3 and v_4. Black dashed lines indicate the initial average concentration. (a')-(d') The free energy curves of α phase and β phase at critical temperatures, colored dashed lines stand for the average concentration of matrix at critical temperatures.

temperature decreases to 640°C, however, the pseudospinodal mechanism can still be activated (inferred from Fig. 9(b')). In addition, as shown in Fig. 9(b), the continuous change of β-stabilizer concentration from initial average value ($c_{initial}$=8.15 %) to the equilibrium one in the α phase (c_e=2.0 %) below 640 °C confirms the existence of pseudospinodal mechanism and the concentration distribution change from a single-peak (under cooling rate v_1, Fig. 9(a)) to triple-peaks (Fig. 9(b)). Thus, the pseudospinodal mechanism, which is the only one operating under this cooling rate, is responsible for generating the UM with fine non-equilibrium α precipitates.

With the continued increase of the cooling rate, e.g., v_1, the short time span at each transformation temperature suppresses the classical nucleation and growth mechanism as well as the pseudospinodal mechanism that requires intermediate-range to long-range diffusion. When the temperature decreases to 540°C, c_0 moves to the right of the matrix composition (Fig. 9(a')), and the congruent transformation mechanism is activated, which is characterized by the lack of any composition change (see Fig. 9(a)).

On the contrary, at cooling rate v_4 (slow cooling), the time span at each transformation temperature is sufficient to allow all the transformation mechanisms to operate. Since the alloy composition is far from c_0 at high temperatures, only the classical nucleation and growth

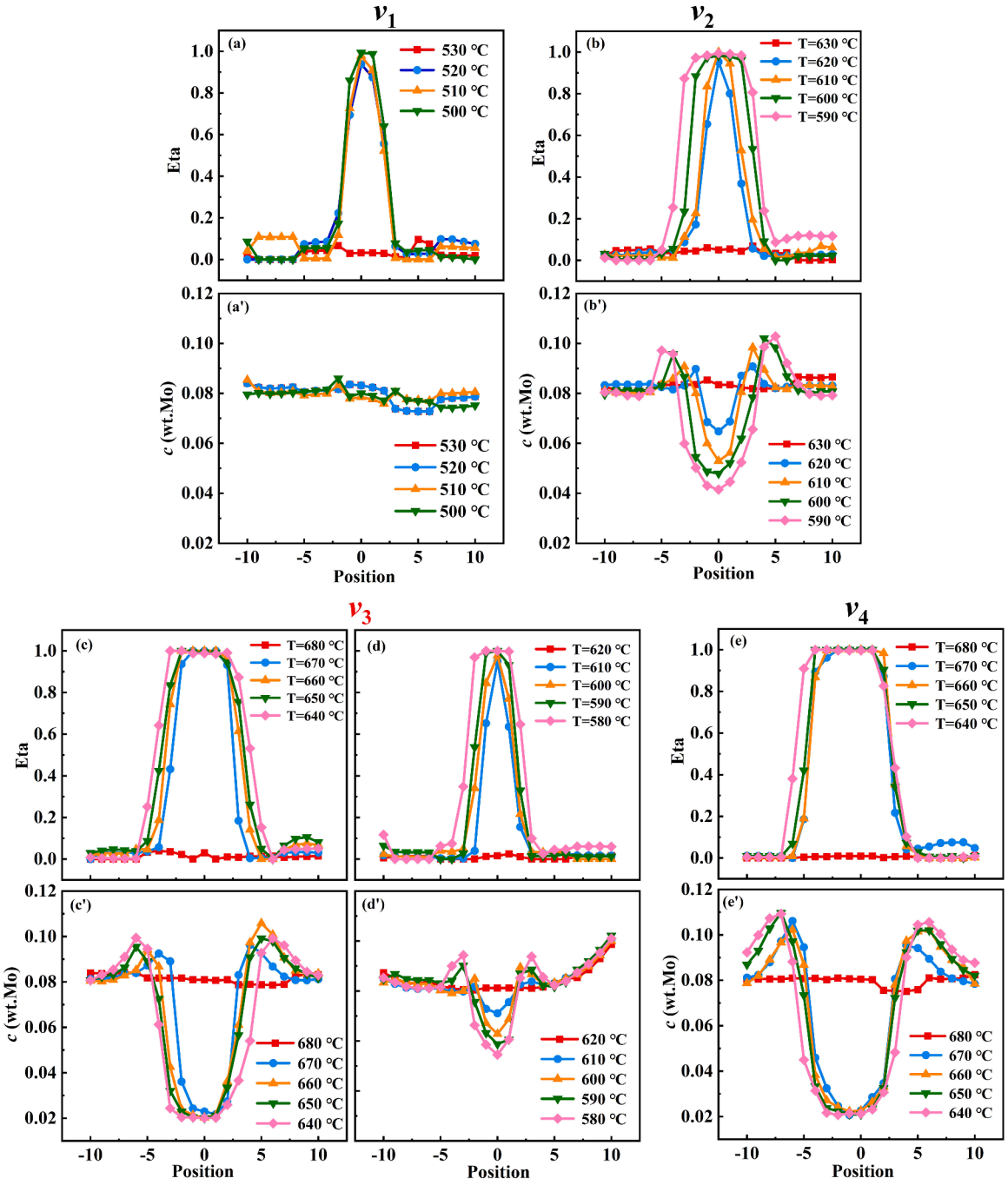

Fig. 10. Temperature evolution of structural order parameter and concentration profiles along the center of supercritical nucleus generated by different cooling rates via different nucleation mechanisms. Temperature evolution of structural order parameter ((a) (b) (d)) and concentration ((a') (b') (d')) of α nucleus formed by pseudospinodal decomposition. Temperature evolutions of the structural order parameter ((c) (e)) and concentration ((c') (e')) of *α* nucleus formed by conventional nucleation and growth.

mechanism can operate, which produces low density coarse α precipitates. Fig. 9(d) indicates that the concentration distribution changes rapidly from unimodal to bimodal at 690 °C, accompanied by a direct jump of the Mo-lean peak to the equilibrium Mo-concentration in the α phase. As temperature further decreases, the bimodal distribution becomes more pronounced, where the Mo-rich peak shifts gradually to the right. The gradual increase in $\Delta c = c_{\beta\_matrix}\text{-}c_0$ beyond 2.5 % leads to the suppression of the pseudospinodal mechanism at lower temperatures. Besides, As the concentration of the matrix increases, the phase transition driving force (ΔG) of classical nucleation and growth decreases, and the nucleation rate decreases. Therefore, a UM with coarse equilibrium α precipitates is generated.

Furthermore, the evolution of the structural order parameter and concentration fields with temperature across supercritical nuclei obtained from the phase field simulations at different cooling rates (Fig. 10) also provides convincing evidence for the different transformation mechanisms activated along the cooling paths. For example, Fig. 10(c), (c'), and (d), (d') differentiate the two different transformation mechanisms activated under v_3. In the high temperature range, the conventional nucleation and growth mechanism operates, in which the structural order parameter and concentration reach their equilibrium values simultaneously (Fig. 10(c) and (c')). In contrast, in the lower temperature range (Fig. 10(d) and (d')), the structural order parameter reaches the equilibrium value instantaneous while the concentration gradually evolves towards equilibrium, indicating that the pseudospinodal mechanism operates. The time evolution of the structural order parameter and concentration fields across a supercritical nucleus under the fast (v_2) and slow cooling rate (v_4) possess only the characteristics of pseudospinodal decomposition (Fig. 10(b) and (b')) and classical nucleation and growth mechanism (Fig. 10(d) and (d')), respectively, leading to the formation of UMs. In addition to the above two precipitation mechanisms, Fig. 10(a) and (a') show the congruent transformation mechanism under v_1. In this case, the structural order parameter at the center of the supercritical nucleus reaches its equilibrium value quickly while the concentration field remains the initial β matrix composition.

5. Conclusion

This work provides a new approach to designing heterogeneous microstructures (HMs) in near-β Ti alloys, aiming to synergistically enhance both strength and ductility. Take the advantages of phase field simulation, a fundamental understanding of various types of precipitate microstructures can be engineered simply by adjusting the linear cooling rate. By decreasing the cooling rate, four distinctive microstructures are produced: congruent α_c, uniform microstructure (UM) with fine α phase, HM with multi-scale α phase, and UM with coarse α phase. Concurrently, the phase transition mechanisms transition gradually from congruent precipitation to pseudospinodal decomposition and then to classical nucleation and growth. The design of HMs, which combines these different transition mechanisms, holds the potential to simultaneously enhance strength and ductility. To provide precise guidance for subsequent experiments, a continuous cooling diagram is constructed for fine, coarse, and bimodal precipitate microstructures in Ti-Mo systems. Experimental validation of the heat treatment schedule to achieve HMs in a commercial Ti-alloy confirms the effectiveness of HM design through cooling rate control. Under a cooling rate of 0.01°C/s, the HMs in Ti55531 exhibit a remarkable strength of 1260 MPa along with a high ductility of up to 14 %. Our work not only elucidates the regularities of microstructure variation and phase transformation mechanisms corresponding to cooling rates but also presents a versatile design concept for HMs applicable to α+β Ti-alloys and other precipitation-hardened alloys. Furthermore, exploring non-linear cooling rates holds promising prospects for future HM designs.

CRediT authorship contribution statement

Mengyuan Hao: Visualization, Methodology, Formal analysis, Writing – original draft, Writing – review & editing. **Dong Wang:** Conceptualization, Visualization, Writing – review & editing. **Yalong Wang:** Methodology, Writing – review & editing. **Tianlong Zhang:** Visualization, Writing – review & editing. **Pei Li:** Methodology, Writing – review & editing. **Yaning Guo:** Writing – review & editing. **Yufeng Zheng:** Conceptualization, Methodology, Writing – review & editing. **Qiaoyan Sun:** Writing – review & editing. **Yunzhi Wang:** Conceptualization, Visualization, Writing – review & editing.

Declaration of competing interest

The authors declare that they have no known competing financial interests or personal relationships that could have appeared to influence the work reported in this paper.

Acknowledgments

DW and MH would like to acknowledge the support from the National Natural Science Foundation of China (Grant No. 52171012), the National Key Research and Development Program of China (Grand No. 2021YFB3702603), the Fundamental Research Funds for the Central Universities (xhj032021015–06) and 111 project (BP2018008). MY would like to acknowledge the support from Key R&D Project in Shaanxi Province (No.2022GY-387). YZ appreciates the financial support from the faculty startup funding from University of North Texas. YW would like to acknowledge the support from the US National Science Foundation under Grant DMR-1923929, which has facilitated this continued international collaboration.

References

[1] C.L. Jia, L.H. Wu, P. Xue, D.R. Ni, B.L. Xiao, Z.Y. Ma, Effect of static annealing on superplastic behavior of a friction stir welded Ti-6Al-4V alloy joint and microstructural evolution during deformation, J. Mater. Sci. Technol. 130 (2022) 112–123.
[2] E.B. Taddei, V.A.R. Henriques, C.R.M. Silva, C.A.A. Cairo, Production of new titanium alloy for orthopedic implants, Mater. Sci. Eng., C 24 (2004) 683–687.
[3] S. Cecchel, L. Montesano, G. Cornacchia, Wear and corrosion characterization of a Ti-6Al-4V component for automotive applications: forging versus selective laser melting technologies, Adv. Eng. Mater. 24 (2022) 2200082.
[4] V. Gheorghita, P. Gumpel, A. Chiru, J. Strittmatter, Future applications of Ni-Ti alloys in automotive safety systems, Int. J. Automotive Tech. 15 (2014) 469–474.
[5] I.V. Okulov, H. Wendrock, A.S. Volegov, H. Attar, U. Kuhn, W. Skrotzki, J. Eckert, High strength beta titanium alloys: new design approach, Mater. Sci. Eng., A 628 (2015) 297–302.
[6] M. Niinomi, Recent research and development in titanium alloys for biomedical applications and healthcare goods, Sci. Technol. Adv. Mater. 4 (2003) 445–454.
[7] X.Y. Liu, P.K. Chu, C.X. Ding, Surface modification of titanium, titanium alloys, and related materials for biomedical applications, Mater. Sci. Eng., R 47 (2004) 49–121.
[8] H. Garbacz, M. Pisarek, K.J. Kurzydlowski, Corrosion resistance of nanostructured titanium, Biomol. Eng. 24 (2007) 559–563.
[9] D. Banerjee, J.C. Williams, Perspectives on titanium science and technology, Acta Mater. 61 (2013) 844–879.
[10] Q.Y. Zhao, Q.Y. Sun, S.W. Xin, Y.N. Chen, C. Wu, H. Wang, J.W. Xu, M.P. Wan, W. D. Zeng, Y.Q. Zhao, High-strength titanium alloys for aerospace engineering applications: a review on melting-forging process, Mater. Sci. Eng., A 845 (2022) 143260.
[11] X. Zhang, H.C. Kou, J.S. Li, F.S. Zhang, L. Zhou, Evolution of the secondary alpha phase morphologies during isothermal heat treatment in Ti-7333 alloy, J. Alloys Compd. 577 (2013) 516–522.
[12] R.P. Shi, T.W. Heo, B.C. Wood, Y.Z. Wang, Critical nuclei at hetero-phase interfaces, Acta Mater. 200 (2020) 510–525.
[13] Y. Ni, A.G. Khachaturyan, From chessboard tweed to chessboard nanowire structure during pseudospinodal decomposition, Nat. Mater. 8 (2009) 410–414.
[14] S. Nag, Y. Zheng, R.E.A. Williams, A. Devaraj, A. Boyne, Y. Wang, P.C. Collins, G. B. Viswanathan, J.S. Tiley, B.C. Muddle, R. Banerjee, H.L. Fraser, Non-classical homogeneous precipitation mediated by compositional fluctuations in titanium alloys, Acta Mater. 60 (2012) 6247–6256.
[15] A. Boyne, D. Wang, R.P. Shi, Y. Zheng, A. Behera, S. Nag, J.S. Tiley, H.L. Fraser, R. Banerjee, Y. Wang, Pseudospinodal mechanism for fine alpha/beta microstructures in beta-Ti alloys, Acta Mater. 64 (2014) 188–197.

[16] B.Z. Jiang, S. Emura, K. Tsuchiya, Microstructural evolution and its effect on the mechanical behavior of Ti-5Al-5Mo-5V-3Cr alloy during aging, Mater. Sci. Eng., A 731 (2018) 239–248.
[17] R. Santhosh, M. Geetha, M.N. Rao, Recent developments in heat treatment of beta titanium alloys for aerospace applications, T. Indian Metals 70 (2017) 1681–1688.
[18] Z.X. Du, S.L. Xiao, L.J. Xu, J. Tian, F.T. Kong, Y.Y. Chen, Effect of heat treatment on microstructure and mechanical properties of a new beta high strength titanium alloy, Mater. Des. 55 (2014) 183–190.
[19] F.J. Gong-Ye, J. Zhou, Q. Zhang, S. Long, Y.T. Zhou, S.S. Li, S.X. Peng, H.P. Deng, J. S. Zhang, Effect of cyclic heat treatment on microstructure and mechanical properties of Ti-5Al-5Mo-5V-3Cr-1Zr alloy, Mater. Res. Express 8 (2021) 076511.
[20] C.W. Huang, Y.Q. Zhao, S.W. Xin, C.S. Tan, W. Zhou, Q. Li, W.D. Zeng, High cycle fatigue behavior of Ti-5Al-5Mo-5V-3Cr-1Zr titanium alloy with lamellar microstructure, Mater. Sci. Eng., Ag 682 (2017) 107–116.
[21] W.H. Liu, H. Deng, H. Chen, L. Zhou, H.Y. Zuo, P. Xu, W.B. Qiu, L.Q. Chen, Y. Q. Wei, Z.X. Xia, H.Q. Peng, J. Tang, Ti-5Al-5V-5Mo-3Cr-1Zr (Ti-55531) alloy with excellent mechanical properties fabricated by spark plasma sintering combined with in-situ aging, Mater. Sci. Eng., A 847 (2022) 143316.
[22] L. Ren, W.L. Xiao, W.Z. Han, C.L. Ma, L. Zhou, Influence of duplex ageing on secondary alpha precipitates and mechanical properties of the near beta-Ti alloy Ti-55531, Mater. Charact. 144 (2018) 1–8.
[23] T.L. Zhang, D. Wang, Y.Z. Wang, Novel transformation pathway and heterogeneous precipitate microstructure in Ti-alloys, Acta Mater. 196 (2020) 409–417.
[24] T.L. Zhang, Z.H. Huang, T. Yang, H.J. Kong, J.H. Luan, A.D. Wang, D. Wang, W. Kuo, Y.Z. Wang, C.T. Liu, In situ design of advanced titanium alloy with concentration modulations by additive manufacturing, Science 374 (2021) 478–482.
[25] A. Zafari, K. Xia, Superior titanium from hybridised microstructures - a new strategy for future alloys, Scr. Mater. 173 (2021) 61–65.
[26] W.G. Zhu, J. Lei, C.S. Tan, Q.Y. Sun, W. Chen, L. Xiao, J. Sun, A novel high-strength beta-Ti alloy with hierarchical distribution of alpha-phase: the superior combination of strength and ductility, Mater. Des. 168 (2019) 107640.
[27] M.Y. Hao, P. Li, X.X. Li, T.L. Zhang, D. Wang, Q.Y. Sun, L.B. Liu, J.S. Li, Y.Y. Cui, R. Yang, D.S. Xu, Heterogeneous precipitate microstructure in titanium alloys for simultaneous improvement of strength and ductility, J. Mater. Sci. Technol. 124 (2022) 150–163.
[28] M.Y. Hao, Y.L. Wang, P. Li, T.L. Zhang, J.M. Zhu, D. Wang, Heterogeneous microstructure enhanced comprehensive mechanical properties in titanium alloys, Jom 73 (2021) 3082–3091.
[29] Y.L. Wang, M.Y. Hao, D.A. Li, P. Li, Q.L. Liang, D. Wang, Y.F. Zheng, Q.Y. Sun, Y. Z. Wang, Enhanced mechanical properties of Ti-5Al-5Mo-5V-3Cr-1Zr by bimodal lamellar precipitate microstructures via two-step aging, Mater. Sci. Eng., A 829 (2022) 142117.
[30] Z.X. Du, S.L. Xiao, Y.P. Shen, J.S. Liu, J. Liu, L.J. Xu, F.T. Kong, Y.Y. Chen, Effect of hot rolling and heat treatment on microstructure and tensile properties of high strength beta titanium alloy sheets, Mater. Sci. Eng., A 631 (2015) 67–74.
[31] H. Deng, L.Q. Chen, W.B. Qiu, Z. Zheng, Y. Tang, Z.D. Hu, Y.Q. Wei, Z.X. Xia, G. M. Le, J. Tang, X.D. Cui, Microstructure and mechanical properties of as-deposited and heat treated Ti-5Al-5Mo-5V-3Cr-1Zr (Ti-55531) alloy fabricated by laser melting deposition, J. Alloys Compd. 810 (2019) 151792.
[32] C.W. Huang, Y.Q. Zhao, S.W. Xin, C.S. Tan, W. Zhou, Q. Li, W.D. Zeng, Effect of microstructure on high cycle fatigue behavior of Ti-5Al-5Mo-5V-3Cr-1Zr titanium alloy, Int. J. Fatigue 94 (2017) 30–40.
[33] C.W. Huang, Y.Q. Zhao, S.W. Xin, W. Zhou, Q. Li, W.D. Zeng, Effect of microstructure on tensile properties of Ti-5Al-5Mo-5V-3Cr-1Zr alloy, J. Alloys Compd. 693 (2017) 582–591.
[34] C.W. Huang, Y.Q. Zhao, S.W. Xin, W. Zhou, Q. Li, W.D. Zeng, C.S. Tan, High cycle fatigue behavior of Ti-5Al-5Mo-5V-3Cr-1Zr titanium alloy with bimodal microstructure, J. Alloys Compd. 695 (2017) 1966–1975.
[35] C. Wu, M. Zhan, Microstructural evolution, mechanical properties and fracture toughness of near beta titanium alloy during different solution plus aging heat treatments, J. Alloys Compd. 805 (2019) 1144–1160.
[36] P. Li, Q.Y. Sun, L. Xiao, J. Sun, Tuning the morphology of Ti-5Al-5Mo-5V-3Cr-1Zr alloy: from brittle to ductile fracture, Mater. Sci. Eng., A 769 (2020) 138487.
[37] X.J. Tian, S.Q. Zhang, H.M. Wang, The influences of anneal temperature and cooling rate on microstructure and tensile properties of laser deposited Ti-4Al-1.5Mn titanium alloy, J. Alloys Compd. 608 (2014) 95–101.
[38] S. Zhu, H. Yang, L.G. Guo, X.G. Fan, Effect of cooling rate on microstructure evolution during alpha/beta heat treatment of TA15 titanium alloy, Mater. Charact. 70 (2012) 101–110.
[39] L. Lei, Q.Y. Zhao, C. Wu, Y.Q. Zhao, S.X. Huang, W.J. Jia, W.D. Zeng, Variant selection, coarsening behavior of alpha phase and associated tensile properties in an alpha plus beta titanium alloy, J. Mater. Sci. Technol. 99 (2022) 101–113.
[40] T. Ahmed, H.J. Rack, Phase transformations during cooling in alpha+beta titanium alloys, Mater. Sci. Eng., A 243 (1998) 206–211.
[41] F.J. Gil, M.P. Ginebra, J.M. Manero, J.A. Planell, Formation of alpha-Widmanstatten structure: effects of grain size and cooling rate on the Widmanstatten morphologies and on the mechanical properties in Ti6Al4V alloy, J. Alloys Compd. 329 (2001) 142–152.
[42] G. Lutjering, Influence of processing on microstructure and mechanical properties of (alpha+beta) titanium alloys, Mater. Sci. Eng., A 243 (1998) 32–45.
[43] D. Nursyifaulkhair, N. Park, E.R. Baek, S. Kim, Influence of cooling rate on volume fraction of alpha massive phase in a Ti-6Al-4V alloy fabricated using directed energy deposition, Mater. Lett. 257 (2019) 126671.
[44] J.H. Dai, J.Y. Xia, L.J. Chai, K.L. Murty, N. Guo, M.R. Daymond, Correlation of microstructural, textural characteristics and hardness of Ti-6Al-4V sheet beta-cooled at different rates, J. Mater. Sci. 55 (2020) 8346–8362.
[45] K.G. Wang, D. Wu, D. Wang, Z.X. Deng, Y.Y. Tian, L.G. Zhang, L.B. Liu, Influence of cooling rate on omega phase precipitation and deformation mechanism of a novel metastable beta titanium alloy, Mater. Sci. Eng., A 829 (2022) 142151.
[46] D. Sharma, D. Parfitt, B. Chen, B. Roebuck, D.A. Venero, S.R. Kada, D. Fabijanic, M. E. Fitzpatrick, Influence of cooling rate on the precipitation kinetics of nanoscale isothermal omega-phase in metastable beta-Ti alloy, Ti-5Al-5Mo-5V-3Cr, J. Alloys Compd. 859 (2021) 157822.
[47] J. Chen, W.L. Xiao, M.S. Dargusch, C.L. Ma, The Dependence of Isothermal omega precipitation on the quenching rate in a metastable beta-Ti Alloy, Sci. Rep. 5 (2015) 14632.
[48] Z.Y. Zheng, L.J. Chai, Z.H. Li, W.J. Huang, L. Tian, Y.F. Wang, L.L. Liu, Effects of beta-cooling rates on microstructural characteristics and hardness of Ti-5Al-5Mo-5V-3Cr-1Fe metastable beta Ti alloy, Mater. Chem. Phys. 276 (2022) 125318.
[49] C. Wu, Y.Q. Zhao, S.X. Huang, Q.Y. Sun, L. Zhou, Effect of cooling rate on a variant selection and microstructure evolution in a near 13 Ti-5Al-3Mo-3V-2Cr-2Zr-1Nb-1Fe alloy, J. Alloys Compd. 841 (2020) 155728.
[50] S.S. Babu, K.M. Miller, M.J. Vitek, A.J.A.M. S., Characterization of the microstructure evolution in a nickel base superalloy during continuous cooling conditions, Acta Mater. 49 (2001) 4149–4160.
[51] Y.H. Wen, B. Wang, P.J. Simmons, Y.J.A. Materialia, A phase-field model for heat treatment applications in Ni-based alloys, Acta Mater. 54 (2006) 2087–2099.
[52] Y.H. Wen, J.P. Simmons, C. Shen, C. Woodward, Y. Wang, Phase-field modeling of bimodal particle size distributions during continuous cooling, Acta Mater. 51 (2003) 1123–1132.
[53] R.P. Kolli, A. Devaraj, A review of metastable beta titanium alloys, Metals (Basel) 8 (2018) 506.
[54] S.Y. Lee, Y. Iijima, K. Hirano, Diffusion of chromium and palladium in beta-titanium, Mater. T. Jim 32 (1991) 451–456.
[55] Y.J. Liu, L.J. Zhang, D. Yu, Computational study of mobilities and diffusivities in bcc Ti-Zr and bcc Ti-Mo alloys, J. Phase Equilib. Diff. 30 (2009) 334–344.
[56] G. Ghosh, Thermodynamic and kinetic modeling of the Cr-Ti-V system, J. Phase Equilib. 23 (2002) 310–328.
[57] R. Shi, N. Ma, Y. Wang, Predicting equilibrium shape of precipitates as function of coherency state, Acta Mater. 60 (2012) 4172–4184.
[58] T.L. Zhang, D. Wang, J.M. Zhu, H. Xiao, C.T. Liu, Y.Z. Wang, Non-conventional transformation pathways and ultrafine lamellar structures in gamma-TiAl alloys, Acta Mater 189 (2020) 25–34.
[59] R. Shi, Y. Wang, Variant selection during alpha precipitation in Ti-6Al-4V under the influence of local stress - A simulation study, Acta Mater. 61 (2013) 6006–6024.
[60] J.H. Zhang, X.X. Li, D.S. Xu, C.Y. Teng, H. Wang, L. Yang, H.T. Ju, H.S. Xu, Z. C. Meng, Y.J. Ma, Y.Z. Wang, R. Yang, Phase field simulation of the stress-induced alpha microstructure in Ti-6Al-4V alloy and its CPFEM properties evaluation, J. Mater. Sci. Technol. 90 (2021) 168–182.
[61] J.O. Andersson, J. Agren, Models for numerical treatment of multicomponent diffusion in simple phases, J. App. Phys. 72 (1992) 1350–1355.
[62] A.A. Wheeler, W.J. Boettinger, G.B. McFadden, Phase-field model for isothermal phase-transitions in binary-alloys, Phys. Rev. A 45 (1992) 7424–7439.
[63] Q. Chen, N. Ma, K.S. Wu, Y.Z. Wang, Quantitative phase field modeling of diffusion-controlled precipitate growth and dissolution in Ti-Al-V, Scr. Mater. 50 (2004) 471–476.
[64] P. Barriobero-Vila, G. Requena, F. Warchomicka, A. Stark, N. Schell, T. Buslaps, Phase transformation kinetics during continuous heating of a beta-quenched Ti-10V-2Fe-3Al alloy, J. Mater. Sci. 50 (2015) 1412–1426.